Assessing surface heat fluxes in atmospheric reanalyses with a decade of data from the NOAA Kuroshio Extension Observatory

Dongxiao Zhang, JISAO/University of Washington, Seattle, Washington, U.S.A.

Meghan F. Cronin, NOAA/Pacific Marine Environmental Laboratory, Seattle, Washington, U.S.A.

Caihong Wen[#&], Yan Xue[#] and Arun Kumar[#]

[#]NOAA/NWS/NCEP/Climate Prediction Center, College Park, Maryland,U.S.A

[&]Innovim, Greenbelt, Maryland,U.S.A

Dai McClurg, JISAO/University of Washington, Seattle, Washington, U.S.A.

Corresponding author: Dongxiao Zhang, JISAO/University of Washington, 7600 Sand Point Way NE, Seattle, WA 98115 (dzhang@uw.edu)

Key Points

• A decade of hourly surface fluxes observed from the NOAA Kuroshio Extension Observatory moored buoy is now available

• Overall surface heat fluxes in CFSR and ERA-I at KEO are significantly improved compared to earlier reanalyses

• Bulk algorithm in CFSR severely overestimates the winter heat release in the Kuroshio and Kuroshio Extension

Index Terms and Key Words

4504, 4576, 3307, 4260, 4262

Air-sea interaction, surface heat flux, NOAA/Ocean Climate Stations, buoy measurements, atmospheric reanalysis

24   **Abstract.** Previous studies have found large biases and uncertainties in the air-sea fluxes from

25   Numerical Weather Prediction model reanalyses, which must be identified and reduced in order to make

26   progress on weather and climate predictions. Here, air-sea heat fluxes from NOAA Kuroshio Extension

27   Observatory (KEO) measurements are used to assess two new reanalyses, NCEP's Climate Forecast

28   System Reanalysis (CFSR) and ECMWF Reanalysis-Interim (ERA-I), suggesting that these two new

29   generation reanalyses have significantly improved. In both reanalyses, all four flux components

30   (sensible and latent heat flux and net longwave and shortwave radiation) are highly correlated with

31   observation, with the correlation of total net surface heat fluxes above 0.96. Although errors of the net

32   surface heat flux have significantly reduced from previous reanalyses, the Root Mean Square Errors

33   (RMSEs) and biases remain high especially for CFSR: the RMSEs of CFSR and ERA-I are reduced by

34   25-30% to 64 and 61 W/m^2 respectively, while biases are reduced by 40-60% to 28 and 20 W/m^2. But

35   CFSR overestimates the winter heat release by 90 W/m^2. The main cause of biases is the latent heat flux,

36   while RMS errors are primarily due to latent heat flux and shortwave radiation errors. Both reanalyses

37   overestimate the wind speed associated with winter storms and underestimate specific humidity in

38   summer. The ERA-I latent heat flux, and its total net surface heat flux, are however closer to

39   observation. It is the bulk algorithm in CFSR that is found to be mainly responsible for overestimates of

40   winter heat release in CFSR.

1. Introduction

41

42   The ocean and atmosphere interact through air-sea fluxes. These fluxes are the most direct ocean

43   climate indicator of how the ocean influences climate and weather and their extremes; and how the

44   atmosphere forces ocean variability. Momentum fluxes (wind stress) drive general ocean circulation,

45   setting up the ocean gyres and current systems that can redistribute heat and properties within the ocean.

46   Air-sea fluxes of heat are the primary mechanism by which the ocean influences the atmosphere. The

47   intense heat release along the western boundary current (WBC) and its extension (WBCE) plays a key

48   role in setting and modulating the upper ocean stratification, mode water formation, and large scale

49   ocean circulations [Qiu et al. 2006; Cronin et al. 2010], as well as biogeochemical processes.

50   In addition to being dynamically important, WBCE regions, and the Kuroshio Extension

51   Observatory (KEO) region in particular, offer a wide range of conditions for testing models. The KEO

52   surface mooring is located in the recirculation gyre south of the Kuroshio Extension (KE). During the

53   quasi-stable periods of the KE, currents can be very weak; during other periods, the site can experience

54   strong currents associated with the meandering jet and drifting eddies. The jets and eddy field can also

55   be associated with strong SST fronts that can organize cloud formation processes and various air-sea

56   interactions. Over the course of a year, the SST variation in WBC, and the KE in particular, can range

57   over 15°C; with smaller variations occurring on time scales down to subdiurnal. Comparison with KEO

58   data thus provides a stringent test for the ability of models to replicate air-sea interactions that are also

59   relevant to many other regions.

60   Atmospheric Reanalysis is an important source for gridded global air-sea flux products that are

61   derived from Numerical Weather Prediction (NWP) models run with a consistent analysis system. There

62   are large uncertainties, however, in air-sea fluxes obtained from atmospheric model analyses and

63   reanalyses, as well as remotely sensed data [*Jiang et al.* 2005; *Kubota et al.* 2008; *Tomita et al.* 2010;

64 *Brunke et al*. 2011]. It is well accepted that these errors must be identified and reduced in order to make

65 progress with weather forecasts and climate projection [*Bourassa et al.* 2013, *Yu et al*. 2013].

66   Errors in the air-sea fluxes in these numerical products can arise due to inadequacies in assimilated

67 data (e.g. satellite measurements that are obscured by clouds, too sparse in situ observations), inadequate

68 parameterizations and bulk algorithms, and inadequate resolution and model dynamics. In some cases,

69 the errors may be dominated by a mean bias, while in other cases the errors may be associated with a

70 particular time scale or dynamical phenomena. Only by understanding the nature of the error can the

71 models be improved. High quality measurements that can be used to calculate the heat fluxes are

72 however difficult to obtain in the WBC region due to strong currents, high winds and high seas. So far,

73 validation of air-sea fluxes in these regions have been mostly based on relatively short records that last

74 about 1 to 2 years, from which not even seasonal cycle can be reliably derived. This limits our

75 understanding of the identified systematic errors in the context of long term mean and seasonal cycles

76 [e.g., *Kubota et al*. 2008; *Tomita et al*.; *Jin and Yu* 2013]. Since 2004, the KEO moored surface buoy has

77 been monitoring the air-sea heat exchanges and upper ocean temperature, salinity and near surface

78 currents [*Cronin et al*. 2008; *Cronin et al*. 2013] in the recirculation gyre just south of the Kuroshio

79 Extension jet. These high-resolution, high-quality mooring measurements thus provide an excellent

80 platform for testing model analyses and reanalyses in this very dynamic region.

81   Using measurements from the first two deployments of KEO (July 2004 - November 2005), *Kubota*

82 *et al*. [2008] evaluated the National Centers for Environmental Prediction (NCEP) / National Center for

83 Atmospheric Research reanalysis (NRA1) and NCEP / Department of Energy reanalysis (NRA2). They

84 found large total net flux biases (Root Mean Square errors) of 49 (77) W/m^2 for NRA1 and 56 (86)

85 W/m^2 for NRA2, with ocean losing too much heat during much of the year mainly caused by errors in

86 latent heat flux. Recently, two new generation reanalyses have been developed: the NCEP Climate

87 Forecasting System Reanalysis (CFSR) and the European Centre for Medium-range Weather Forecasts

88 (ECMWF) Reanalysis Interim project (ERA-I). Figure 1 however shows large differences of total net

89 surface heat flux in the Kuroshio and Kuroshio Extension (KKE) region between CFSR and ERA-I.

90   This study will use a decade of KEO moored buoy data to evaluate the air-sea exchanges of heat in

91 the two newer generation reanalyses. In the following, KEO measurements and calculation of the heat

92 fluxes using bulk algorithm will be briefly described in Section 2; in Section 3 the KEO fluxes will be

93 used to validate the CFSR and ERA-I reanalyses. These bulk flux data are now being made publicly

94 available at http://www.pmel.noaa.gov/OCS/data/fluxdisdel/ and this paper is intended to describe

95 details of these flux data. Section 4 will investigate the causes of the latent flux bias, which is found to

96 be mainly responsible for the large bias of total net heat flux in the CFSR; conclusions and suggestions

97 will be made in Section 5.

98

99 **2. Data and Methods**

100 **2.1 Heat Fluxes from KEO Measurements**

101   KEO is located in the KE's recirculation gyre at 32.3°N, 144.5°E (Figure 1), and is currently the

102 only heavily instrumented surface mooring in any WBC/WBCE regime that has a long-term record of

103 air-sea fluxes [*Cronin et al.* 2010]. KEO measures the meteorological state variables and ocean

104 conditions, including biogeochemical variables, upper ocean temperature and salinity, and near-surface

105 currents. It thus is capable of monitoring the air-sea exchanges of heat, moisture, momentum and carbon

106 dioxide; ocean acidification; and upper ocean variability associated with air-sea interaction.

107   The net surface heat flux, Q_{net}, has both radiative and turbulent components:

108             $Q_{net} = Q_{sw,net} - Q_{lw,net} - Q_{lat} - Q_{sen}$ *(1)*

109 where $Q_{sw,net}$ *and* $Q_{lw,net}$ are the net shortwave and longwave radiation at the air-sea interface:

110 $$Q_{sw,net} = (1 - \alpha)\,SWR \qquad\qquad (2)$$

111 $$Q_{lw,net} = \varepsilon\,(LWR - \sigma T_s^4) \qquad\qquad (3)$$

112 *SWR* and *LWR* are the measured incoming solar and longwave radiation, T_s is the measured surface

113 temperature of the ocean; α is the sea surface albedo derived from the International Satellite Cloud

114 Climatology Project (ISCCP, http://isccp.giss.nasa.gov/projects/browse_fc.html), ε is the broadband

115 emissivity (0.98), and σ is the Stefan-Boltzmann constant (5.67×10^{-8} W m^{-2} K^{-4}).

116   Air-sea turbulent fluxes can be represented in terms of a bulk aerodynamic formula. In particular, the

117 latent (Q_{lat}) and sensible (Q_{sen}) heat fluxes can be expressed as:

118 $$Q_{lat} = \rho_a\,L\,C_e\,S\,(q_a - q_s) \qquad\qquad (4)$$

119 $$Q_{sen} = \rho_a\,C_p\,C_T\,S\,(T_a - T_s) \qquad\qquad (5)$$

120 where ρ_a is the atmospheric surface density, $S^2 = |(\boldsymbol{U_a} - \boldsymbol{U_s})|^2 + w_g^2$, $\boldsymbol{U_a} - \boldsymbol{U_s}$ is the hourly wind speed

121 relative to the ocean surface current, w_g is the wind gustiness, (T_a-T_s) is the air-sea temperature

122 difference, and q_a is the surface specific humidity, while q_s is the saturated specific humidity at the sea

123 surface temperature. The "state variables" needed for the bulk fluxes include hourly averaged wind

124 speed and direction, ocean surface currents, air and sea surface temperature, and humidity, and are all

125 directly measured by KEO. C_e and C_T are the transfer coefficients for the latent and sensible bulk heat

126 fluxes, which are determined through state-of-the-art COARE v3.0b bulk algorithm. The version 2.5

127 COARE algorithm [*Fairall et al.* 1996a] was formulated for the Tropics using data from the Tropical

128 Ocean Global Atmosphere (TOGA) Coupled Ocean Atmosphere Response Experiment (COARE).

129 Tuned for low wind speed regions, it introduced several novel features, including a warm layer and cool

130 skin model to extrapolate bulk sea surface temperature (SST) to the skin [*Fairall et al.* 1996b] and a

131 gustiness component to account for the difference between hourly wind speed computed from the

132 averaged vector components (conventional method) and that computed from averaging the scalar wind

133 speeds directly (appropriate for flux calculation). Version 3.0b [*Fairall et al.* 2003] made the algorithm

134 applicable to global regions with high wind speeds. We therefore used COARE 3.0b to derive Q_{lat} and

135 Q_{sen} in *(1)-(5)*.

136   Air temperature, humidity, and SST are measured every 10 minutes; and winds are measured for 2

137 minutes every 10 minutes. Incoming solar and longwave radiation are recorded as 1-or-2-minute

138 averages. Near surface currents at either 5 m, 15m, or in some cases 35m, have had different sampling

139 schemes through the years ranging 10 minutes before 2007 and 20 minutes afterwards. Full high

140 resolution data are available only after the mooring is recovered. Since 2014, hourly averages of all state

141 variables are transmitted to the lab, and thus the bulk fluxes can be computed in real time (available

142 within 24 hours) with COARE 3.0b. Between September 2007 and June 2014, most of the state

143 variables including winds, air temperature, relative humidity, sea surface salinity and temperature

144 observed hourly were submitted to the Global Telecommunication System (GTS) in near real time and

145 most of the time when satellites were available. Since June 2014, with the upgrade of satellite

146 communication system, all hourly state variables and radiation measurements from KEO have been

147 submitted to the GTS in near real time all the time.

148   The air-sea fluxes used in this analysis are from 2004 to 2014; the period during which both ERA-I

149 and CFSR were available when this study started. The fluxes are however available to the research

150 community and public in real time through our new OCS Flux Display and Delivery Web Page

151 developed as part of this study (http://www.pmel.noaa.gov/OCS/data/fluxdisdel/). Both hourly and

152 daily-averaged fluxes are provided. While hourly fluxes are based on hourly means of observed

153 variables as per COARE 3.0b, daily fluxes are the daily averages of their hourly counterparts. Figure 2 is

154 directly obtained from the web page, showing the hourly and daily fluxes in *(1)*. Turbulent heat fluxes

155 (Q_{lat} and Q_{sen}) and net longwave radiation ($Q_{lw,net}$) are the mechanism by which the ocean heats the

156 atmosphere in the WBC/WBCE region. Positive values of these three cooling terms in (1) therefore

157 indicate heat is released from the ocean. For net shortwave radiation ($Q_{sw,net}$), the heating term in *(1)*,

158 and the total net surface heat flux (Q_{net}), positive values are defined as the heat gained by the ocean

159 (downward), while negative as the heat released from the ocean to the atmosphere (upward). *Kubota et*

160 *al*. [2008] presented an extensive analysis of measurement errors in turbulent fluxes based on the pre-

161 and post-deployment calibrations and instrument random errors following upon *Freitag et al.* [2005] and

162 *Cronin et al.* [2006]. The total measurement errors of daily average Q_{lat} and Q_{sen} are estimated to be 12

163 W/m^2 and 5 W/m^2 respectively, which also include 10% random error due to uncertainties of bulk

164 COARE algorithm in high wind conditions [*Fairall et al*. 2003]. The measurement errors of *LWR* and

165 *SWR* are 4 W/m^2 and 3 W/m^2.

166 **2.2 The New Generation Reanalyses**

167 The Climate Forecast System Reanalysis (CFSR) [*Saha et al.* 2010] was designed and executed as a

168 global, high-resolution coupled atmosphere–ocean–land surface–sea ice system to provide the best

169 estimate of the state of the ocean-atmosphere coupled system from 1979 to 2010. Since 2011, the CFSR

170 has been updated in real time. New features of the CFSR include 1) coupling of the atmosphere and

171 ocean during the generation of the 6-h guess field, 2) an interactive sea ice model, and 3) assimilation of

172 satellite radiances by the Gridpoint Statistical Interpolation (GSI) scheme over the entire period. The

173 CFSR global atmosphere resolution is ~38 km (T382) with 64 levels extending from the surface to 0.26

174 hPa. The global ocean's latitudinal spacing is 0.25° at the equator, extending to a global 0.5° beyond the

175 tropics, with 40 levels to a depth of 4737 m. CFSR atmospheric, oceanic, and land surface output

176 products are available at an hourly time resolution for some selected variables.

177 Currently, CFSR is the only reanalysis based on a coupled ocean-atmosphere-land data assimilation

178 system. The ocean data assimilation is accomplished by 3D-Var with data input including global

179 observation of subsurface temperature (T) profiles and synthetic salinity (S) profiles based on

180 climatological T-S relationship [*Xue et al.* 2011]. To provide a stronger constraint at the ocean-

181 atmosphere interface, the modeled SST is however relaxed to the daily 1/4° NOAA OI SST (Reynolds et

182 al. 2007), a blend of satellite AVHRR/AMSR and in situ measurements. The air-sea fluxes in the

183 coupled CFSR are computed in the model with the bulk algorithm similar to those in NRA1 and NRA2,

184 but using *Zeng et al.* [1998] roughness lengths for heat and moisture which is generally considered as a

185 simplified version of COARE 2.5 bulk algorithm.

186   The ERA-Interim (ERA-I) is an 'interim' reanalysis in preparation for the next-generation extended

187 reanalysis to replace ERA-40. ERA-I (Dee et al. 2011), however, has many improvements over ERA-40,

188 including a much higher resolution model (T255, ~79km) with improved atmospheric physics and the

189 12-h 4DVar assimilation system with improvements to the handling of data biases and the background

190 error constraint. While the stability function of the bulk algorithm for calculating air-sea fluxes in ERA-I

191 are based on *Holtslag and de Bruin* [1988] and *Dyer* [1974], the roughness length for momentum is

192 directly computed from the coupled ocean wave model in operational model and reanalysis.

193   Both reanalyses assimilated various satellite measurements, including high resolution satellite winds,

194 in addition to in situ atmospheric measurements. Compared to previous generation atmospheric

195 reanalyses, which have coarse resolution (~200km, for example NCEP reanalyses and ERA40), the

196 CFSR and ERA-I have higher resolution to better resolve many aspects of atmospheric processes, such

197 as storms [*Hodges et al.* 2011]. Due to the coarse resolution, the Sea Surface Temperature (SST) in the

198 earlier generation reanalyses deviates largely from the in situ buoy measurements, and is responsible for

199 a large part of the differences between buoy measured fluxes and reanalyses [*Kubota et al.* 2008; *Cronin*

200 *et al.* 2006]. The SST in CFSR and ERA-I however compare favorably with the KEO SST (Figure 3),

201 with both correlations higher than 0.99, Root Mean Square errors of 0.5°C, and biases within 0.1°C.

202   Daily fluxes in the two reanalyses are calculated from 6-hourly means. KEO is a slack-line mooring

203   in a strong-current WBC/WBCE regime, the surface buoy therefore has a large drift circle of up to 6 km

204   radius from its anchor location, which is changed with each deployment year. To compare with the KEO

205   measurements, 6-hourly reanalysis fluxes are interpolated to the instantaneous buoy locations tracked by

206   the Global Positioning System. As in *Kubota et al.* [2008], assessment of the reanalysis products will be

207   provided by the correlation of daily fluxes of measurements and reanalysis, the Root Mean Square

208   Errors (RMSE) measuring the magnitude of daily differences, and the bias measuring the mean

209   differences. Because of the long-term measurements at KEO, for the first time we are able to reliably

210   estimate seasonal cycle of the flux components, and to compare them to reanalyses. The CFSR also

211   provides hourly "state variables" that can be used to calculate turbulent fluxes using COARE 3.0b bulk

212   algorithms as for KEO observation, and to test the bulk algorithms used in CFSR. Throughout the paper,

213   all statistics (correlation, RMSE, and bias) are calculated from daily timeseries, even though sometimes

214   low-pass filtered timeseries are presented in figures to better show the differences. These statistics are

215   tabulated in Table 1a and b, and are compared in the following to those in Table 1c and d for NRA1 and

216   NRA2 [*Kubota et al.* 2008]. Note that Kubota et al's comparisons were based on a shorter time period

217   (July 2004- November 2005). To make sure that the longer period used to construct Table 1a and b does

218   not favor better comparisons, Table 1e and f are included for reference to show the comparison of CFSR

219   and ERA-I with the KEO observation in the same period as in Table 1c and d. Overall the statistics

220   presented in the Table 1e and f are similar to those in Table 1a and b, suggesting the relative

221   improvements of the two new reanalyses compared to NRA1 and NRA2 are robust regardless of the

222   comparison periods.

223

224   **3. Comparison of Heat Fluxes**

225   **3.1 Radiation Heat Fluxes**

226   The net longwave radiation $Q_{lw,net}$ at KEO is predominantly positive (losing heat from the ocean in

227   *(1))*, changing from close to 0 in summer to over 100 W/m^2 in winter (Figure 2b). Statistics of the

228   comparison between KEO and CFSR/ERAI are shown in Table 1a and 1b. Compared to NRA1 and

229   NRA2 (Table 1c and 1d, reproduced from [Kubota et al. 2008]), the two new reanalyses show

230   significant improvement in terms of correlation. Even when seasonal cycles are removed, the

231   correlations are significantly high (> 95% significance level), suggesting a good correspondence

232   between the reanalyses and observation in synoptic weather events, which are dominant contributors to

233   the variability and degrees of freedom in the anomaly timeseries. The biases are also low,

234   indistinguishable from KEO measurement errors. The RMSEs however remain above 10 W/m^2. Since

235   SST in the two new reanalyses are highly correlated with the KEO measurements (Figure 3), the RMSEs

236   are mainly induced by the downward longwave radiation (*LWR)*. This is confirmed by the comparison of

237   directly measured *LWR* by KEO and its counterpart in the reanalyses (Table 1 a and b, Figure 4 a and c).

238   Even with low biases and high correlations with observation, the reanalysis *LWR*s have large RMSEs.

239   While the CFSR tends to overestimate the *LWR* in winter and underestimate in summer, the ERA-I tends

240   to underestimate it in later winter to early spring though within the standard errors of computed seasonal

241   cycles (Figure 7). The differences between the seasonal cycles of *LWR* are small, within 10 W/m^2

242   throughout the year.

243   The net shortwave radiation is the main heating source of the ocean at KEO as in *(1)*, noting that

244   positive values of $Q_{sw,net}$ in Figure 2 refer to downward heat flux into the ocean. While hourly net

245   shortwave radiation at KEO change dramatically in a day from 0 to over 1000 W/m^2 following the sun,

246   daily means range from a few 10 W/m^2 in winter to 300 W/m^2 in summer. $Q_{sw,net}$ in both reanalyses are

247   significantly correlated with that based on KEO measurements, though with very high RMSEs (Table 1

248   a and b). The CFSR has a much larger bias than ERAI (10 W/m^2 in CFSR vs. 2 W/m^2 in ERAI). These

249   errors are mainly caused by *SWR* since observed albedo values in *(2)* are small ranging from 0.05-0.11

250   with a clear seasonal cycle (Figure 5). *Kubota et al.* [2008] reported that although NRA1 simulates the

251   correct amplitude of albedo seasonal cycle compared to the ISCCP climatology, its absolute albedo

252   values, ranging from 0.14 to 0.2, are 100% larger than observed. NRA2 on the other hand has a much

253   smaller seasonal change of albedo, ranging from 0.06-0.08. Figure 5 compares the albedo in CFSR and

254   ERAI reanalyses with two satellite products, the ISCCP climatology and daily Cloud and the Earth's

255   Radiation System (CERES) (ceres.larc.nasa.gov). It is interesting to note that the albedo seasonal cycle

256   in both CFSR and ERA-I are much smaller than ISCCP, but closer to CERES. Details of the differences

257   in ISCCP and CERES will be addressed in a separate study. However the small absolute values of

258   albedo at KEO coupled with their anti-phase relation with *SWR* means that the impacts of the differences

259   in albedo on $Q_{sw,net}$ are small. Like NRA2, CFSR and ERAI simulate correctly the phase of seasonal

260   cycle, but with much smaller amplitude. The larger albedo difference in winter (~0.03 between the

261   reanalyses and ISCCP) would only result in less than 3 W/m^2 difference in $Q_{sw,net}$ due to the relatively

262   weak *SWR* during winter.

263   Since variability of $Q_{sw,net}$ is largely determined by SWR, directly measured *SWR* at KEO is

264   compared to the reanalyses (Figure 4). The instantaneous differences can be up to over 100 W/m^2

265   inducing the large RMSEs (Table 1 a and b) although the correlations of the reanalyses and observation

266   are significant. To better illustrate the differences, Figure 6 zooms in the timeseries in 2005. The

267   timeseries follow each other closely even on synoptic weather time scales suggesting that the reanalyses

268   successfully capture the weather events, which can change the *SWR* by up to 200 W/m^2 in just a few

269   days during spring and summer. The good correspondence between the synoptic weather events in the

270   reanalyses and observed timeseries is consistent with the significantly high correlations between them

271   even when the dominating seasonal cycles are removed (Table 1a and 1b). It is therefore the difference

272   in amplitudes of these weather events that result in the large RMSEs of *SWR* on the order of 40 W/m^2 in

273   both reanalyses. Both reanalyses show overestimates of *SWR* in spring 2005 and underestimates of *SWR*

274   in summer in 2005, similar to Kubota et al.'s assessment of NRA1 and NRA2 using the first 15 months

275   of KEO measurements. But the seasonal cycle derived from longer timeseries suggest that CFSR

276   overestimates the *SWR* in both spring and early summer, while ERA-I underestimates in late summer

277   and early fall (Figure 7).

278   The CFSR overestimate of *SWR* and underestimate of *LWR* in much of the spring and summer is

279   consistent with the negative cloud bias in the KEO region [*Wang et al.* 2011]. Because of the

280   compensation of *LWR* and *SWR* biases, the total downward radiative flux of CFSR is within the standard

281   errors of the KEO seasonal cycle in most of the year (Figure 7c). On the other hand, the large negative

282   bias of total downward radiative flux in ERA-I in late summer and early fall is significant. However, the

283   annual mean, the winter and summer means of ERA-I *SWR* and *LWR* are in excellent agreement with the

284   KEO measurement for ERA-I (Table 2). The summer mean positive bias of 19 W/m^2 (Table 2) in CFSR

285   *SWR* due to cloud biases is particularly large, and is mostly responsible for the 10 W/m^2 *SWR* annual

286   mean bias (Table 1a and Table 2).

287

288   **3.2 Turbulent Heat Fluxes**

289   Q_{lat} and Q_{sen} are the other two cooling terms in *(1)*, both having large seasonal variations with close

290   to 0 in summer and maximum heat release in winter (Figure 2). While Q_{sen} winter heat release is

291   comparable to $Q_{lw,net}$, winter cooling from Q_{lat} is much larger, more than Q_{sen} and $Q_{lw,net}$ combined. Q_{sen}

292   in both CFSR and ERA-I compare well with the KEO observations, with very high correlation and low

293   biases (Table 1 a and b). The RMSEs of CFSR and ERA-I Q_{sen} are 14 and 13 W/m^2 respectively.

294   Compared to NRA1 and NRA2, the two new generation reanalyses have similar or higher correlations

295   with KEO observation, but also have significantly lowered RMSEs and biases. The errors are however

296   concentrated in winter season (Figure 8c), which leads to the more substantial systematic winter bias of

297   more than 20 W/m^2 cooling in the seasonal cycle (Figure 7d).

298   Q_{lat} in CFSR and ERAI are more problematic (Figure 8 b and d). Although they are very highly

299   correlated with the KEO observation (0.96 for CFSR and 0.94 for ERAI), they have large RMSEs and

300   biases (Table 1 a and b). The instantaneous differences of reanalyses and observation can be more than

301   100 W/m^2, especially for CFSR (Figure 8d). Both reanalyses are biased to lose more heat than they

302   should throughout most of the year for CFSR and in summer and early fall for ERA-I, which is clearly

303   seen in the seasonal cycle (Figure 7e). The CFSR bias (31 W/m^2) is particularly pronounced with its

304   enhanced systematic winter bias of more than 70 W/m^2. Compared to NRA1 and NRA2, both the two

305   new reanalyses however have made substantial progress of improving Q_{lat}, with higher correlations,

306   lower RMSEs and biases (Table 1 a and b vs. Table 1 c and d). More detailed diagnostics on what

307   caused the still exceedingly large biases in the new reanalyses, particularly for CFSR, will be presented

308   later in Section 4.

309

310   **3.3 Total Net Heat Fluxes**

311   The total net surface heat flux Q_{net} at KEO, as the sum of the warming term ($Q_{sw,net}$) and cooling

312   terms ($Q_{lw,net}$, Q_{sen}, and Q_{lat}), have extraordinary seasonal extremes with up to 300 W/m^2 warming to the

313   ocean in summer and up to 1000 W/m^2 cooling in winter (Figure 9a). Although the correlations (Table 1

314   a and b) between the reanalyses and KEO observation are very high (even when large seasonal cycles

315   are removed), the instantaneous differences can be more than 200 W/m^2 (Figure 9b). The RMSEs are 64

316   W/m^2 for CFSR and 61 W/m^2 for ERAI, while biases are 28 W/m^2 for CFSR and 20 W/m^2 for ERAI.

317   Though still large, these errors are much smaller than NRA1 and NRA2 (Table 1 c and d). The large

318   RMSEs are mainly contributed by the errors in *SWR* and Q_{lat}, while the large cooling biases are due to

319   Q_{lat}. The ERA-I biases are mostly in late summer and early fall (Figure 7f), induced by overestimates of

320   latent heat loss (Figure 7e) and underestimates of *SWR* (Figure 7b). The CFSR, however, has the largest

321   bias of up to 90 W/m^2 during winter in the seasonal cycle (Figure 7). If a negative 90 W/m^2 is

322   distributed over a mixed layer of 50-m, it could induce a cooling of about 2.2°C within two months.

323   KEO is located at the center of North Pacific Subtropical Mode Water (STMW) formation region. If the

324   CFSR fluxes are used to force an ocean circulation model, such a large cooling bias at this region would

325   generate significant biases on the STMW formation and therefore the heat/gas uptake, as well as the

326   large scale ocean circulation in the North Pacific.

327

328   **4. Biases in Latent Heat Flux**

329   The mechanism responsible for the large winter heat release in the Kuroshio and Kuroshio Extension

330   region is the cold winter outbreaks that bring cold and dry continental air from the northwest over the

331   warm Kuroshio water. This is clearly seen in Figure 10 a and b, showing the maximum winter cooling of

332   Q_{lat} which contributes to most of the Q_{net} (Figure 1). These synoptic scale winter weather outbreaks are

333   associated with the winter storms in the North Pacific Storm Track [*Bond and Cronin* 2008, *Konda et al*.

334   2010]. Figure 10 c and d show that the composite cooling anomalies correspond to the southwest

335   quadrant of the storms when the centers of the storms are located to the northeast of KEO. During these

336   events, the anomalous winds (Figure 10 c and d) are similar to the winter mean (Figure 10 a and b) in

337   terms of both strength and direction passing over the Kuroshio and KEO. Figure 10 also suggests that

338   the anomalous cooling events measured by KEO have spatial scales of more than several hundred

339   kilometers. It is interesting to note that although ERA-I has similar wind to CFSR in winter mean

340   (Figure 10a and b) and anomalous cooling events (Figure 10c and d, Figure 12), the associated Q_{lat} in

341   ERA-I are much weaker than CFSR.

342   According to (4), the "state variables" that determine Q_{lat} are wind speed (relative to ocean

343   currents), specific humidity of the air $q_{a,}$ and saturated specific humidity q_s at sea surface temperature.

344   Since q_s (largely determined by SST) in the two reanalyses are close to observation (not shown, but see

345   SST in Figure 3) and speed of ocean currents are an order of magnitude smaller than wind speed, we

346   compare the wind speed and q_a in the reanalyses with KEO observation in Figure 11, where KEO

347   measured variables are adjusted to the same height as reanalysis variables using COARE algorithm.

348   Both reanalysis wind speeds are highly correlated with observation (0.83 for CFSR and 0.84 for ERA-I),

349   and both tend to overestimate the wind speeds especially during winter and with similar magnitude. The

350   RMSE and bias of CFSR wind are 2.1 m/s and 1.0 m/s respectively, while those of ERA-I are 1.9 m/s

351   and 0.7 m/s. q_a in the reanalyses are even more highly correlated with observation (with correlation of

352   both higher than 0.99). The RMSE and bias of q_a in CFSR are 0.8 and -0.4 g/kg respectively, while

353   those in ERAI are 0.9 and -0.5 g/kg. *Kubota et al.* [2008] found that q_a in NRA1 and NRA2 was

354   overestimated in winter and underestimated in summer so that the errors in q_a contribute most to errors

355   of Q_{lat}. q_a in the two new reanalyses, however, are much better during winter, though there is still a clear

356   underestimate of q_a during summer (Figure 11). Figure 12 zooms in winter 2013 and shows that q_a in

357   CFSR and ERAI follow almost exactly the KEO measurement, and both reanalyses overestimate the

358   wind speeds by similar magnitude during anomalous synoptic weather events corresponding to the

359   composite storm pattern (Figure 10). Thus it may be surprising that while the CFSR overestimates Q_{lat}

360   by 50-100 W/m^2, Q_{lat} in ERAI is much closer to observation.

361   Another factor that determines Q_{lat} according to *(4)* is the transfer coefficient C_e that is calculated

362   through bulk algorithm. Since CFSR also provides hourly data we can calculate Q_{lat} using CFSR "state

363   variables" and COARE 3.0b and compare it with KEO latent heat flux calculated the same way.

364   Compared to Figure 13a, Figure 13b shows that using COARE 3.0b improves the CFSR Q_{lat}

365   dramatically: the correlation with observation rises from 0.96 to 0.97; the RMSE reduces from 46 to 32

366   W/m^2; the bias reduces from 31 to 18 W/m^2 (Table 3). So by using the COARE 3.0b bulk algorithm

367   with CFSR state variables, the calculated latent heat flux $Q_{lat,coare}$ is comparable or better than ERA-I.

368   To test the influence of wind bias on Q_{lat} calculation in the bulk algorithm, the observed KEO winds

369   are used to substitute for the CFSR winds (Figure 13c). The calculated Q_{lat} with COARE algorithm and

370   observed wind ($Q_{lat,coare,wind}$) shows only minor correction with respect to $Q_{lat,coare}$ (Table 3). The

371    $Q_{lat,coare,wind}$ correlation with observation is increased to 0.98 from 0.97 (for $Q_{lat,coare}$); the RMSE and bias

372   of $Q_{lat,coare,wind}$ are reduced to 25 W/m^2 and 15 W/m^2 from 32 W/m^2 and 18 W/m^2 respectively (for

373    $Q_{lat,coare}$). To test the influence of q_a bias on Q_{lat}, the observed KEO q_a is used to substitute for the CFSR

374   q_a (Figure 13d). The calculated Q_{lat} with COARE algorithm and observed q_a ($Q_{lat,coare,qa}$) shows only

375   minor improvement in correlation and RMSE but a relatively large bias reduction with respect to

376    $Q_{lat,coare}$ (Table 3). The $Q_{lat,coare,qa}$ correlation with observation is 0.98 and the RMSE is reduced to 26

377   W/m^2, comparable to the improvement from wind-substitute case $Q_{lat,coare,wind}$. But the bias of $Q_{lat,coare,qa}$

378   is further reduced to 7 W/m^2, another 11 W/m^2 reduction from $Q_{lat,coare}$, suggesting the importance of

379   reducing q_a summer biases in the reanalyses (Figure 11c and 11d).

380

5. Summary and conclusions

382   Heat release from the Kuroshio and Kuroshio Extension (KKE) to the mid-latitude atmosphere is an

383   important conduit for poleward heat transport in the global energy balance, and is a major mechanism

384 for the ocean to influence the atmosphere. Exchanges of air-sea fluxes also help determine the upper

385 ocean stratification and play a key role in the North Pacific STMW formation, thereby influencing the

386 heat and gas uptake and the large scale ocean circulation. Earlier generation NWP reanalyses (NRA1

387 and NRA2) have been shown to have alarmingly large RMS errors in the net surface heat flux of more

388 than 77 W/m^2 and bias of more than 49 W/m^2 in the KKE region. These studies were based on the first

389 two deployments of the NOAA Ocean Climate Station (OCS) KEO buoy with a total record of 15

390 months; a time series that is now over 10 years in length. OCS buoys measure upper ocean properties

391 and state variables from which air-sea fluxes can be computed; fluxes from the KEO buoy data provide

392 a very challenging test for NWP due to the large range of meteorological and oceanic conditions

393 experienced there.

394 In this study we use a decade of KEO measurements to evaluate surface heat fluxes in two newer

395 generation reanalyses, the NCEP CFSR and ECMWF ERA-I, which have large difference of total net

396 surface heat flux during winter in the Kuroshio and Kuroshio Extension (Figure 1). It is found that both

397 the two new reanalyses have significantly improved in representation of surface heat fluxes compared to

398 NRA1 and NRA2 in this region. In both new reanalyses, all four flux components (sensible and latent

399 heat flux and net longwave and shortwave radiation) are highly correlated with observation, with the

400 correlation of total daily net surface heat fluxes above 0.96 (Table 1). Correlations are also high (> 95%

401 significance level) even when the large seasonal cycles are removed, consistent with the good

402 correspondence between the synoptic weather events in reanalyses and observation. Although errors of

403 the net surface heat flux Q_{net} have significantly reduced from previous reanalyses, the RMSEs and biases

404 remain high. The RMSEs of Q_{net} in CFSR and ERA-I are 64 and 61 W/m^2 respectively, compared to 77

405 and 85 W/m^2 in NRA1 and NRA2 [*Kubota et al.* 2008]. The biases of Q_{net} in CFSR and ERA-I are 28

406 and 20 W/m^2 respectively, compared to 49 and 56 W/m^2 in NRA1 and NRA2. However there is still an

407 alarmingly large cooling bias of 90 W/m^2 in winter Q_{net} of CFSR. The Q_{net} in ERA-I in winter is closer

408 to KEO observation, but its late summer and early fall biases are close to 40 W/m^2 (Figure 7f).

409   Among the four flux components of Q_{net}, low errors of net longwave radiation $Q_{lw,net}$ at KEO in both

410 reanalyses (Table 1) are mainly caused by the downward longwave radiation LWR which are close to

411 observation within 10 W/m^2 throughout the seasonal cycle (Figure 7). Sensible heat flux Q_{sen} in CFSR

412 and ERA-I are also reasonably reproduced, though both show amplified cooling bias of ~20 W/m^2 in

413 winter. The errors from both net shortwave radiation $Q_{sw,net}$ and latent heat flux Q_{lat} contribute to the

414 large RMSEs of Q_{net} , while Q_{lat} is the main cause of large cooling biases of Q_{net}. The downward

415 shortwave radiation SWR, that dominates the $Q_{sw,net}$ variability, is overestimated in CFSR in both spring

416 and summer, while in ERA-I it is overestimated in spring but underestimated in late summer and early

417 fall (Figure 7b). Q_{lat} in both reanalyses are biased to lose more heat than they should be throughout most

418 of the year for CFSR and in summer and early fall for ERA-I, as clearly seen in the seasonal cycle

419 (Figure 7e). The CFSR Q_{lat} bias is particularly worrisome with its large winter bias of more than 70

420 W/m^2, responsible for most of the 90 W/m^2 bias of Q_{net} in winter.

421   It is further found that Q_{lat} winter heat release in CFSR is much larger than in ERA-I in the entire

422 Kuroshio and Kuroshio Extensions region (Figure 10a and b). Such a large winter bias in net surface

423 heat flux would have severe consequences when used to force an ocean circulation model. Composite

424 analysis of anomalous cooling events observed at KEO suggests that the anomalous coolings are

425 associated with synoptic winter storms and cold air outbreaks that bring cold dry continental air over the

426 warm Kuroshio water. Both CFSR and ERA-I overestimate the wind speed associated with the winter

427 storms and underestimate the specific humidity in summer. But it is the bulk algorithm that is most

428 responsible for the large bias of Q_{lat} in CFSR particularly for winter. It is therefore recommended that

429   heat fluxes calculated from CFSR state variables and a better bulk algorithm are used to force the ocean

430   models, rather than the fluxes directly from the CFSR.

431   Although CFSR and ERA-I have shown significant improvement compared to earlier reanalyses at

432   the Kuroshio and Kuroshio Extension region, they both have large global heat imbalance with 13 W/m^2

433   and 8 W/m^2 heat flux biases, respectively, when integrated globally [*Valdivieso et al* 2015; *Josey et al*.

434   2013]. The global heat budget of NRA1 and NRA2, on the other hand, are close to being balanced with

435   2-3 W/m^2 globally integrated biases. In addition, a number of variables including radiation fluxes and

436   winds in CFSR suffered a noticeable shift around 2000 likely due to the changes of observing systems

437   and change of schemes in assimilating the data from those observations [*Saha et al.* 2010; *Xue et al.*

438   2011; *Wang et al.* 2011]. Caution should be exercised if CFSR fluxes before 2000 are used to drive

439   ocean models. More comparisons with direct observations like this one in other parts of the ocean and

440   on long term variations of air-sea fluxes are needed to understand and quantify the reanalysis biases and

441   to eventually improve the reanalysis products.

442   One recently discovered caveat in the ERA-I air-sea fluxes is the localized anomalies ("bull's-eyes")

443   associated with the ERA-I's assimilation of Tropical Atmosphere Ocean (TAO) moored buoy

444   observations [*Josey et al.* 2014]. These localized anomalies are particularly strong in the 2m specific

445   humidity q_a, as well as the latent heat flux Q_{lat} and net surface flux Q_{net}. OCS moorings have been

446   designated as the flux reference buoys. And we have been requesting the reanalysis community not to

447   assimilate the OCS data, but to use our data for validation purposes. Special World Meteorology

448   Organization (WMO) reference codes have been assigned and placed the OCS data in the encouraged-

449   to-withhold list among the data distributed by the GTS. Localized anomalies in ERA-I similar to those

450   in the tropical Pacific are not found in the KEO region (Figure 10), suggesting that KEO data is not

451   assimilated. We also had direct communications with the NCEP to discourage the OCS data from being

452 assimilated in the CFS. As summarized below, q_a biases are identified in both CFSR and ERA-I at KEO,

453 and need to be corrected to further improve the reanalysis fluxes. But we like to second the *Josey et al.*

454 [2014] recommendation that "A balance needs to be achieved between assimilating enough data to

455 improve the reanalysis representation of atmospheric variability and withholding enough to enable valid

456 evaluations to be carried out.". This certainly needs close communication between the observation,

457 reanalysis, and diagnosis communities.

458 Overestimation of Q_{lat} has been a long standing problem in reanalyses that have been diagnosed by a

459 series of studies on the previous generation reanalyses [*Josey* 2001; *Moore and Renfrew* 2002; *Sun et al.*

460 2003; *Jiang et al.* 2005; *Cronin et al.* 2006; *Tomita and Kubota* 2006; *Kubota et al.* 2008] in various

461 parts of the ocean. The comparison of earlier KEO data with NRA1 and NRA2 [*Kubota et al.* 2008] led

462 to three recommendations: 1) use higher resolution global SST products based on satellite microwave

463 measurements at all-weather conditions; 2) reduce large biases in the model simulations of specific

464 humidity in winter and summer; and 3) improve bulk algorithms in the NWP model for the air-sea flux

465 calculation. Both CFSR and ERA-I have adopted the merged high resolution SST with microwave

466 measurements included as the boundary condition for their atmospheric models. Overall, they showed

467 excellent agreement with the SST measured by KEO (Figure 3) with correlations higher than 0.99, even

468 though the high resolution SST missed a few cold events in winter (less than 10 days in the entire KEO

469 record). This is a significant improvement compared to coarse relation SST products used in NRA1 and

470 NRA2 [*Kubota et al.* 2008]. The large over-estimates of winter q_a in NRA1 and NRA2 have been

471 significantly improved in CFSR and ERA-I (Figure 11 c and d), but under-estimates of q_a in warm

472 season still exist. Further improvement of q_a in CFSR could potentially reduce Q_{lat} bias by 11 W/m^2 and

473 RMSE by 6 W/m^2 (Table 2). Our study reiterates the importance of appropriate bulk algorithms in

474   calculating the latent heat flux in NWP reanalyses, which remains as the most influential factor causing

475   large biases of Q_{lat} in CFSR (Table 2).

476   One goal of the NOAA OCS buoys, as part of the air-sea flux reference sites, is to provide high

477   quality long term baseline dataset to evaluate global air-sea flux products from reanalyses and satellite

478   products. This study only evaluates two of the new reanalyses. There are several other products (e.g.,

479   JRA, MERRA, 20CR see https://reanalyses.org/atmosphere/overview-current-reanalyses) are available

480   for comparison. To facilitate air-sea interaction research and assessment of air-sea fluxes in NWP

481   reanalyses and other flux products, we have developed the OCS Flux Display and Delivery Web Page

482   (http://www.pmel.noaa.gov/OCS/data/fluxdisdel/), from which computed hourly and daily fluxes can be

483   viewed and downloaded in real time (Figure 2).

484   It worth mentioning that the biases identified here are referred to the reanalysis difference with

485   respect to the COARE algorithm derived mooring flux estimates. The COARE 3.0b, which is based on

486   more than 5000 direct covariance flux measurements over the global ocean, is generally accepted as the

487   more accurate among available bulk algorithms [*Brunke et al.* 2003]. More high-quality direct flux

488   measurements in the Kuroshio and Kuroshio Extension region are however justifiable to further improve

489   the accuracy of air-sea fluxes derived from buoy measurements.

490

496 Agreement NA10OAR4320148, Contribution No. 2645. PMEL contribution number 4464. Data are

497 available at http://www.pmel.noaa.gov/OCS/data/fluxdisdel/.

498

499 **References**

500

501 Bond, N.A., Cronin, M.F.(2008), Regional weather patterns during anomalous air–sea fluxes at the

502 Kuroshio Extension Observatory (KEO). J. Climate 21, 1680–1697, doi: 10.1175/2007JCLI1797.1.

503 Bourassa, M. A. et al. (2013), High-Latitude Ocean and Sea Ice Surface Fluxes: Challenges for Climate

504 Research, Bull. Am. Meteorol. Soc., 94(3), 403–423, doi:10.1175/BAMS-D-11-00244.1.

505 Brunke, M. A., C. W. Fairall, X. Zeng, L. Eymard, and J. A. Curry (2003), Which bulk aerodynamic

506 algorithms are least problematic in coupled ocean surface turbulent fluxes? J. Clim., 16, 619– 634.

507 Brunke, M. A., Z. Wang, X. Zeng, M. Bosilovich, and C.-L. Shie (2011), An assessment of the

508 uncertainties in ocean surface turbulent fluxes in 11 reanalysis, satellite-derived, and combined global

509 datasets, *Journal of Climate*, *24*(21), 5469-5493.

510 Cronin, M.F., Fairall, C.W., McPhaden, M.J (2006), An assessment of buoy-derived and numerical

511 weather prediction surface heat fluxes in the tropical Pacific. J. Geophys. Res. 111, C06038,

512 doi:10.1029/2005JC003324.

513 Cronin, M. F., N. Bond, J. Booth, H. Ichikawa, T. M. Joyce, K. Kelly, M. Kubota, B. Qiu, C. Reason,

514 M. Rouault, C. Sabine, T. Saino, J. Small, T. Suga, L. D. Talley, L. Thompson, R. A. Weller (2010),

515 Monitoring ocean-atmosphere interactions in western boundary current extensions. In Proceedings of

516 the "OceanObs'09: Sustained Ocean Observations and Information for Society" Conference (Vol. 2),

517 Venice, Italy, 21-25 September 2009, Hall, J. Harrison, D. E., and Stammer, D., Eds., ESA

518 Publication WPP-306, doi:10.5270/OceanObs09.cwp.20.

519   Cronin, M. F., N. A. Bond, J. T. Farrar, H. Ichikawa, S. R. Jayne, Y. Kawai, M. Konda, B. Qiu, L.

520   Rainville, H. Tomita (2013), Formation and erosion of the seasonal thermocline in the Kuroshio

521   Extension recirculation gyre. DSR II, 85, 62-74, doi:10.1016/j.dsr2.2012.07.018.

522   Dee, D. P. et al. (2011), The ERA-Interim reanalysis: configuration and performance of the data

523   assimilation system, Q. J. R. Meteorol. Soc., 137(656), 553–597.

524   Dyer, A. J. (1974), A review of flux-profile relationships. *Bound. Layer Meteor.*, 7, 363–372.

525   Fairall, C. W., E. F. Bradley, D. P. Rogers, J. B. Edson, and G. S. Young (1996), Bulk parameterization

526   of air–sea fluxes in TOGA COARE. J. Geophys. Res., 101, 3747–3767.

527   Fairall, C. W., E. F. Bradley, J. S. Godfrey, G. A. Wick, J. B. Edson, and G. S. Young, (1996), Cool skin

528   and warm layer effects on the sea surface temperature. J. Geophys. Res., 101, 1295–1308.

529   Fairall, C.F., Bradley, E.F., Hare, J.E., Grachev, A.A., Edson, J.B., (2003), Bulk parameterization of air-

530   sea fluxes: Updates and verification for the COARE algorithm. J. Climate 16, 571–591.

531   Freitag, H. P., T. A. Sawatzky, K. B. Ronnholm, and M. J. McPhaden (2005), Calibration procedures

532   and instrumental accuracy estimates of next generation ATLAS water temperature and pressure

533   measurements, NOAA Tech. Memo. OAR PMEL-128, 22 pp., Pac. Mar. Environ. Lab., NOAA,

534   Seattle, Wash.

535   Hodges, K. I., R. W. Lee, and L. Bengtsson (2011), A Comparison of Extratropical Cyclones in Recent

536   Reanalyses ERA-Interim, NASA MERRA, NCEP CFSR, and JRA-25, J. Clim., 24(18), 4888–4906,

537   doi:10.1175/2011JCLI4097.1.

538   Holtslag, A. A. M., and H. A. R. de Bruin (1988), Applied modeling of the nighttime surface energy

539   balance over land. *J. Appl. Meteor.*, 27, 689–704.

540   Jiang, C.-L., M. F. Cronin, K. A. Kelly, and L. Thompson (2005), Evaluation of a hybrid satellite and

541   NWP based turbulent heat flux product using TAO buoys. J. Geophys. Res., 110, C09007,

542   doi:10.1029/2004JC002824.

543   Jin, X., and L. Yu. (2013), Assessing high-resolution analysis of surface heat fluxes in the Gulf Stream

544   region, J. Geophys. Res., 118, doi:10.1002/jgrc.20386.

545   Josey, S. A. (2001), A comparison of ECMWF, NCEP-NCAR, and SOC surface heat fluxes with

546   moored buoy measurements in the subduction region of the northeast Atlantic, J. Clim., 14, 1780–

547   1789.

548   Josey SA, Gulev S, Yu L (2013), Exchanges through the ocean surface. In: Siedler G, Griffies S, Gould

549   J, Church J (eds) Ocean circulation and climate, 2nd edn. A 21st century perspective. Academic Press,

550   International Geophysics Series, vol 103, pp 115–140.

551   Josey, S. A., L. Yu, S. Gulev, X. Jin, N. Tilinina, B. Barnier, and L. Brodeau (2014), Unexpected

552   impacts of the Tropical Pacific array on reanalysis surface meteorology and heat fluxes, Geophys.

553   Res. Lett., 41, 6213–6220, doi:10.1002/2014GL061302.

554   Konda, M., H. Ichikawa, H. Tomita, and M. F. Cronin (2010), Surface heat flux variations across the

555   Kuroshio Extension as observed by surface flux buoys. J. Climate, 23, 5206-5221.

556   Kubota, M., Iwabe, N., Cronin, M.F., Tomita, H. (2008), Surface heat fluxes from the NCEP/NCAR and

557   NCEP/DOE reanalyses at the KEO buoy site. J. Geophys. Res. 113, C02009,

558   doi:10.1020/2007JC004338.

559   Moore, G. W. K., and I. A. Renfrew (2002), An assessment of the surface turbulent heat fluxes from the

560   NCEP-NCAR reanalysis over the western boundary currents, J. Clim., 15, 2020– 2037.

561 Qiu, B., P. Hacker, S. Chen, K. A. Donohue, D. R. Watts, H. Mitsudera, N. G. Hogg, and S. R. Jayne

562   (2006), Observations of the Subtropical Mode Water evolution from the Kuroshio Extension System

563   Study. J. Phys. Oceanogr. 36, 457–473.

564 Reynolds, Richard W., Thomas M. Smith, Chunying Liu, Dudley B. Chelton, Kenneth S. Casey,

565   Michael G. Schlax, 2007: Daily High-Resolution-Blended Analyses for Sea Surface Temperature. J.

566   Climate, 20, 5473–5496.

567 Saha, S. et al. (2010), The NCEP Climate Forecast System Reanalysis, Bull. Am. Meteorol. Soc., 91(8),

568   1015–1057, doi:10.1175/2010BAMS3001.1.

569 Sun, B., L. Yu, and R. A. Weller (2003), Comparison of surface meteorology and turbulent heat fluxes

570   over the Atlantic NWP model analyses versus moored buoy observations, J. Clim., 16, 679– 695.

571 Tomita, H., Kako, S., Cronin, M.F., Kubota, M., 2010. Preconditioning of the wintertime mixed layer at

572   the Kuroshio Extension Observatory. J. Geophys. Res. 115, C12053, doi:10.1029/2010JC006373.

573 Tomita, H., and M. Kubota (2006), An analysis of the accuracy of Japanese Ocean Flux data sets with

574   use of Remote sensing Observations (J-OFURO) satellite-derived latent heat flux using moored buoy

575   data, J. Geophys. Res., 111, C07007, doi:10.1029/2005JC003013.

576 Valdivieso, M., et al. (2015), An assessment of air–sea heat fluxes from ocean and coupled reanalyses.

577   Clim. Dyn., DOI 10.1007/s00382-015-2843-337, 1601-1620.

578 Wang W, Xie P, Yoo SH, Xue Y, Kumar A, Wu X (2010), An assessment of the surface climate in the

579   NCEP Climate Forecast System Reanalysis. Clim. Dyn., 37, 1601-1620.

580 Xue, Y., B. Huang, Z.Z. Hu, A. Kumar, C. Wen, D. Behringer, S. Nadiga (2011), An Assessment of

581   Oceanic Variability in the NCEP Climate Forecast System Reanalysis. Clim. Dyn., 37, 2511-2539.

582 Yu, L., K. Haines, M. Bourassa, M. Cronin, S. Gulev, S. Josey, S. Kato, A. Kumar, T. Lee, and D.

583   Roemmich.   Towards   achieving   global   closure   of   ocean   heat   and   freshwater   budgets:

584   Recommendations for advancing research in air-sea fluxes through collaborative activities. In Report

585   of the CLIVAR/GSOP/WHOI Workshop on Ocean Syntheses and Surface Flux Evaluation, Woods

586   Hole, Massachusetts, 27-30 November 2012, WCRP Informal/Series Rep. No. 13/2013, ICPO

587   Informal Rep. 189/13, 42 pp., 2013.

588

589

590

591

592

593

594

595

596

597

598

599

600

601

602

603

604

605

606   Table 1a: Comparison of flux components between KEO and CFSR. Correlations after seasonal cycles

607   removed are in parentheses.

CFSR	$Q_{sw,net}$	SWR	$Q_{lw,net}$	LWR	Q_{lat}	Q_{sen}	Q_{net}
Correlation	0.88	0.88 (0.74)	0.88	0.94 (0.84)	0.96 (0.87)	0.96 (0.90)	0.97 (0.87)
RMS Error	43	47	13	13	46	14	64
Bias	10	10	4	-2	31	3	-28

608

609   Table 1b: Comparison of flux components between KEO and ERA-I. Correlations after seasonal cycles

610   removed are in parentheses.

ERA-I	$Q_{sw,net}$	SWR	$Q_{lw,net}$	LWR	Q_{lat}	Q_{sen}	Q_{net}
Correlation	0.85	0.86 (0.71)	0.89	0.95 (0.84)	0.94 (0.83)	0.94 (0.85)	0.96 (0.84)
RMS Error	43	43	12	12	38	13	61
Bias	4	2	4	-2	17	4	-20

611

612

613

614

615

616

617

618

619

620

621   Table 1c: Comparison of flux components between KEO and NRA1 (reproduced from Kubota et al.)

NRA1	$Q_{sw,net}$	SWR	$Q_{lw,net}$	LWR	Q_{lat}	Q_{sen}	Q_{net}
Correlation	0.80	0.80	0.79	0.91	0.92	0.93	0.93
RMS Error	48	52	15	15	48	20	77
Bias	1	17	1	1	38	9	-49

622

623   Table 1d: Comparison of flux components between KEO and NRA2 (reproduced from Kubota et al.)

NRA2	$Q_{sw,net}$	SWR	$Q_{lw,net}$	LWR	Q_{lat}	Q_{sen}	Q_{net}
Correlation	0.88	0.88	0.78	0.90	0.91	0.94	0.94
RMS Error	38	41	15	16	62	23	85
Bias	-5	4	-6	8	60	7	-56

624

625   Table 1e: Comparison of flux components between KEO and CFSR during July 2004-November 2005

CFSR	$Q_{sw,net}$	SWR	$Q_{lw,net}$	LWR	Q_{lat}	Q_{sen}	Q_{net}
Correlation	0.89	0.89	0.80	0.94	0.97	0.97	0.98
RMS Error	36	39	13	12	35	10	46
Bias	7	7	2	-1	25	1	-20

626

627   Table 1f: Comparison of flux components between KEO and ERA-I during July 2004-November 2005

ERA-I	$Q_{sw,net}$	SWR	$Q_{lw,net}$	LWR	Q_{lat}	Q_{sen}	Q_{net}
Correlation	0.92	0.91	0.88	0.97	0.96	0.97	0.97
RMS Error	31	34	10	9	34	9	51
Bias	2	1	3	-2	20	4	-24

628   Table 2: Annual Mean (DJF Winter Mean) [JJA Summer Mean] values of flux components in KEO

629   observation, CFSR and ERA-I reanalyses.

	SWR	*LWR*	Q_{lat}	Q_{sen}	Q_{net}
KEO	171 (97) [243]	375 (339) [410]	135 (232) [38]	25 (62) [0]	-57 (-291) [+140]
CFSR	181 (91) [262]	373 (347) [405]	166 (282) [65]	28 (77) [-3]	-85 (-343) [+138]
ERA-I	173 (99) [244]	373 (339) [409]	152 (242) [67]	29 (72) [2]	-77 (-298) [+121]

630

631   Table 3: Comparison of KEO latent heat flux Q_{lat} vs. CFSR Q_{lat}, $Q_{lat,coare}$, $Q_{lat,coare,wind}$, and $Q_{lat,coare,qa}$

632   (see text for details).

CFSR	Q_{lat}	$Q_{lat,coare}$	$Q_{lat,coare,wind}$	$Q_{lat,coare,qa}$
Correlation	0.96	0.97	0.98	0.98
RMS Error	46	32	25	26
Bias	31	18	15	7

633

634

635

636

637

638
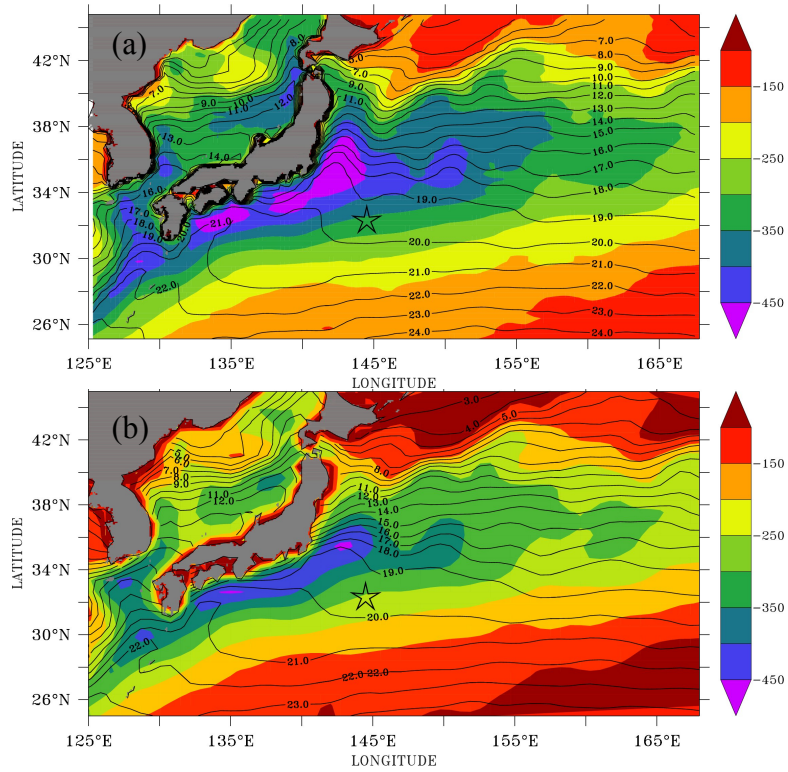
Figure 1. 2004-2014 mean net surface heat flux (color shade) and sea surface temperature (line contours)

in winter (December-January-February) in two reanalyses: (a) NCEP CFSR; (b) ERA-I. Negative

values mean that the ocean is losing heat to the atmosphere. KEO location is marked by the star.

642
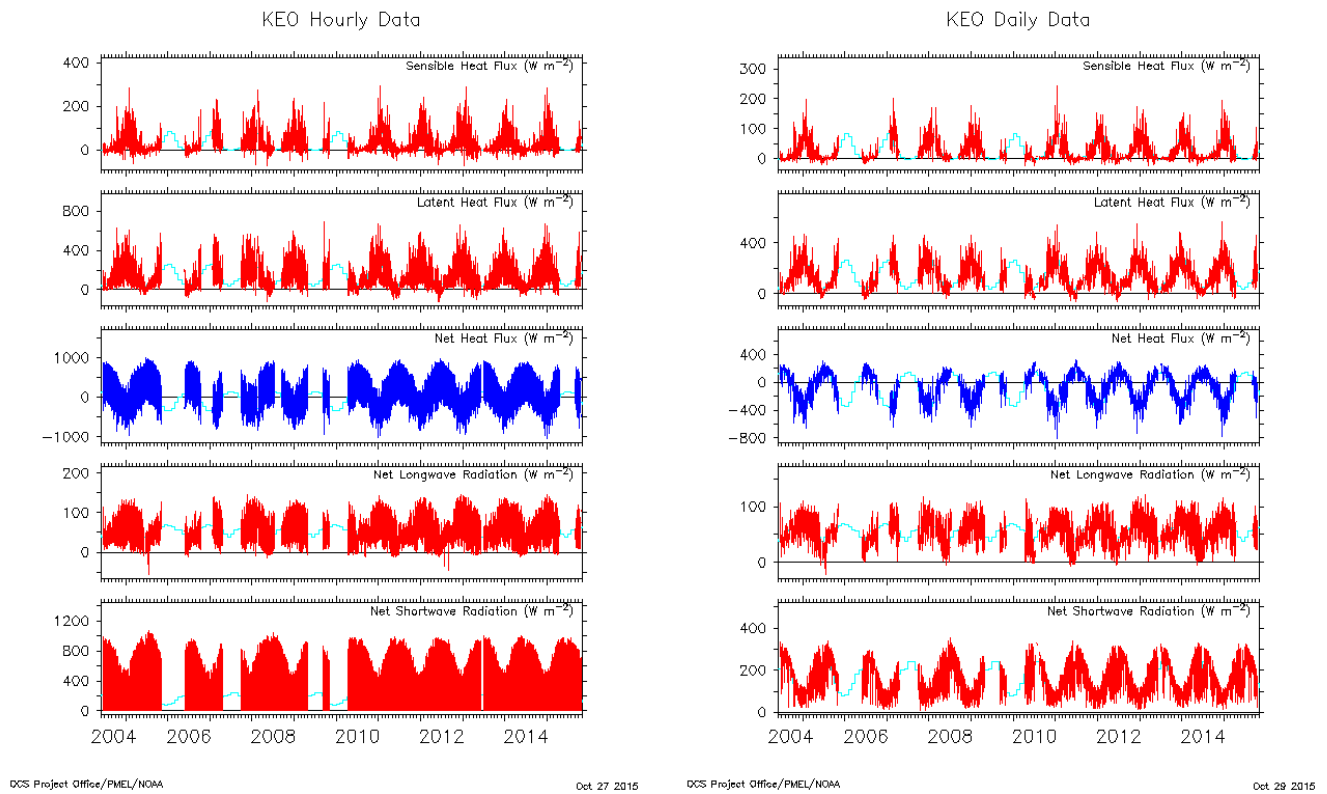
Figure 2. Hourly and daily heat flux components in *(1)* as measured by KEO. The cyan curve in each

sub-plot represents the climatology as defined in http://pmel.noaa.gov/ocs/climatology.

651
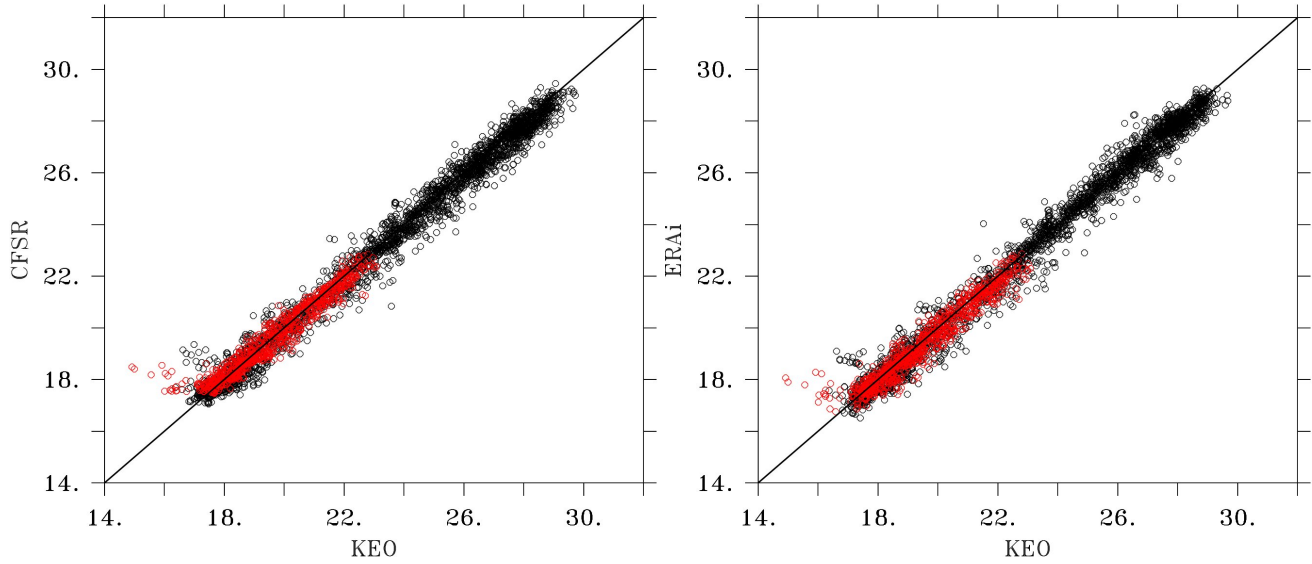
Figure 3: Scatter plot of daily SST measured at KEO and in CFSR and ERA-I reanalyses. Data points in

winter are shown in red.

654

655

656

657

658

659

660

661

662

663

664

665

666
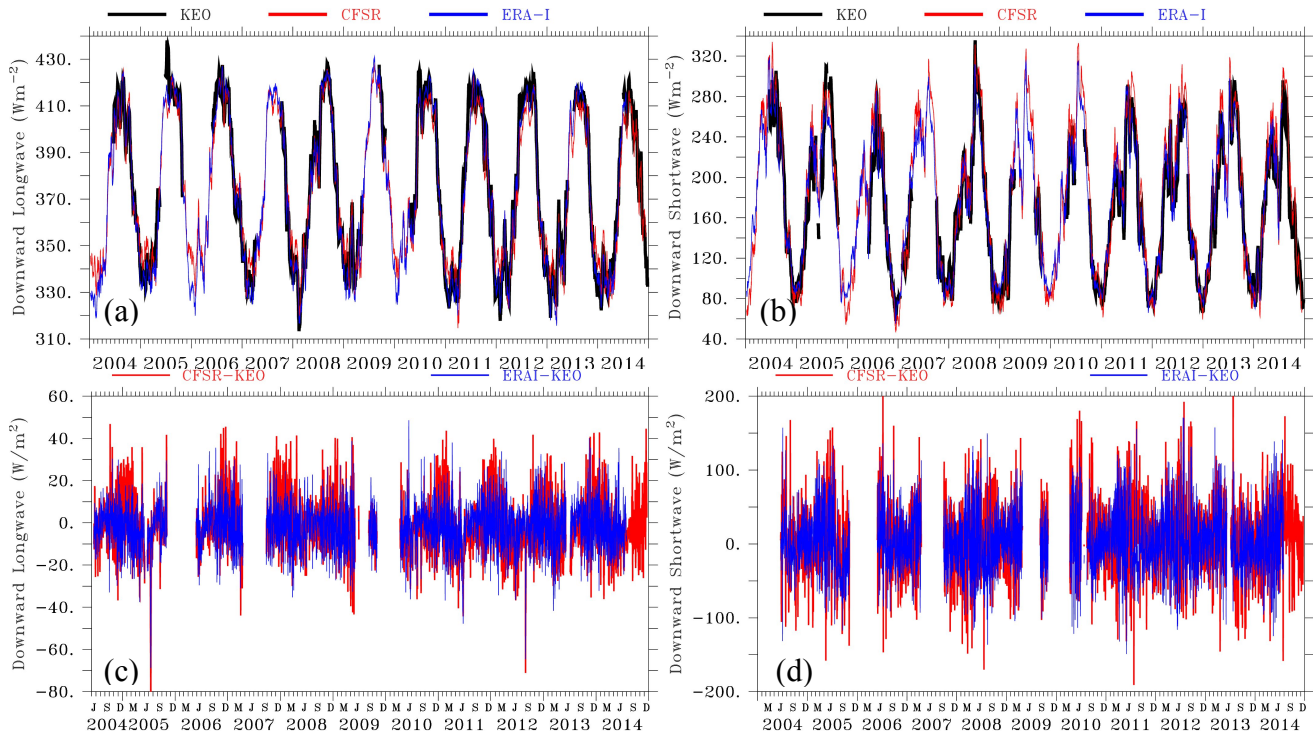
Figure 4. (a) and (b) Downward longwave and shortwave radiation measured by KEO, compared to the CFSR and ERA-I reanalyses (15-day lowpass filtered to better show the timeseries); (c) and (d) Differences of daily CFSR and ERA-I downward shortwave and longwave radiation with KEO measurements.
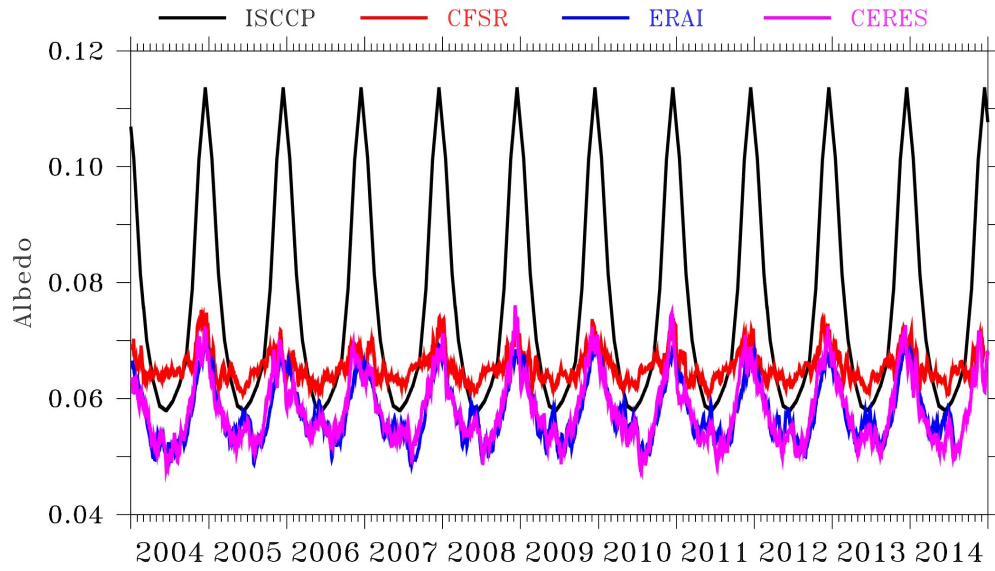
672   Figure 5: Comparison of albedos at KEO in the two reanalyses (CFSR and ERA-I) and two satellite

673   products (ISCCP and CERES).

674

675

676

677

678

679

680

681
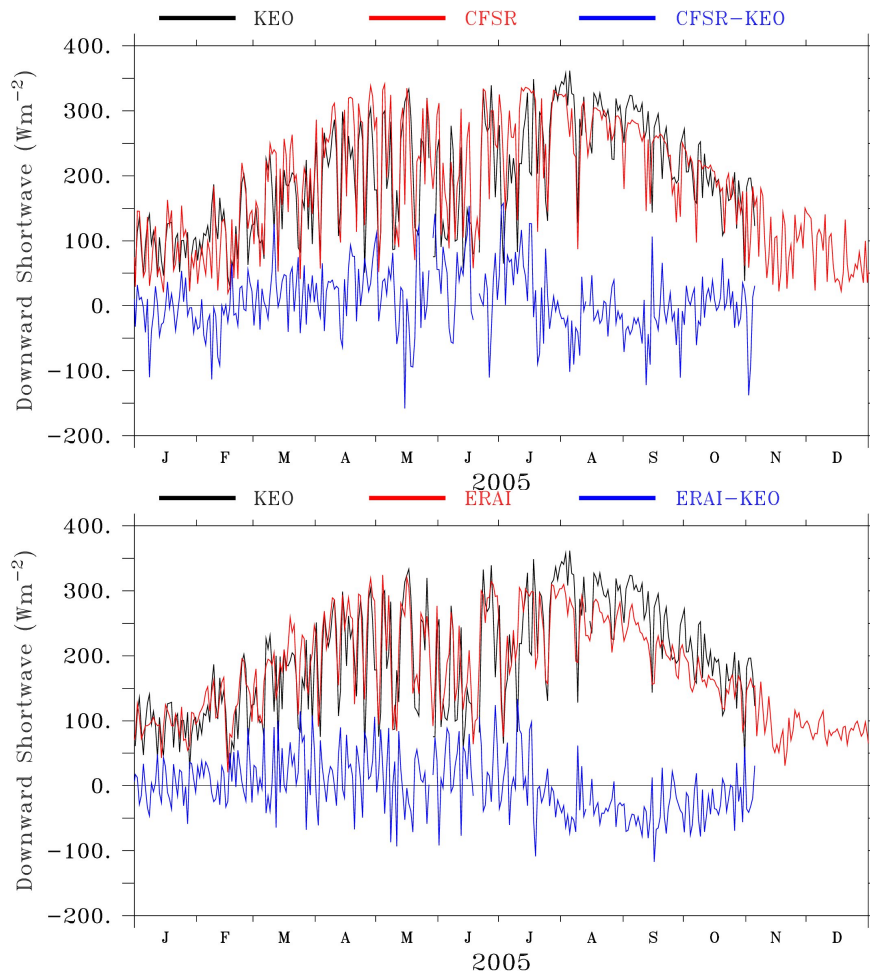
682

683

684

685   Figure 6. Downward daily shortwave radiation measured by KEO and in CFSR and ERA-I, and their

686   differences, during 2005.
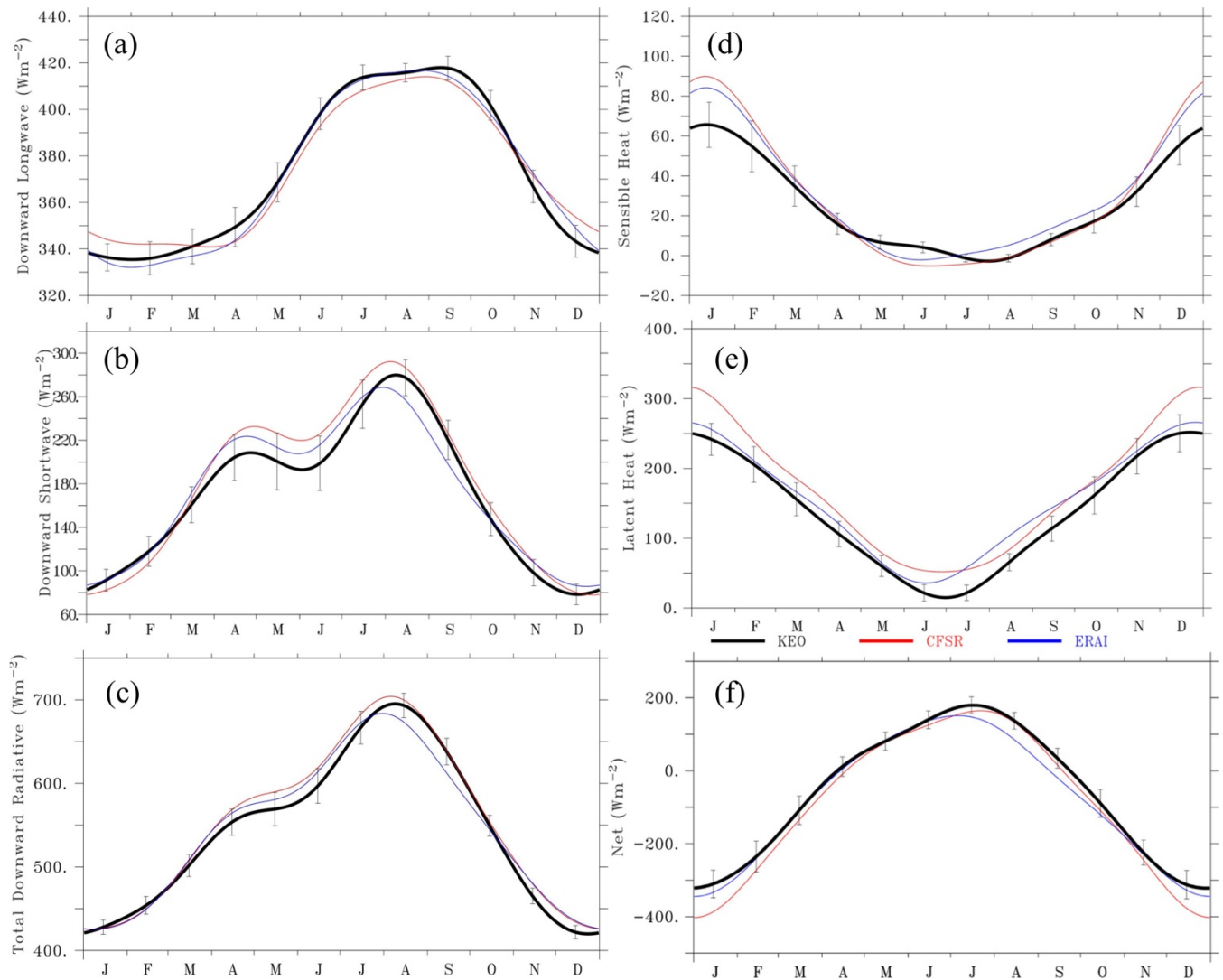
Figure 7: Seasonal cycle of downward longwave and shortwave radiation (a) and (b), total downward longwave and shortwave radiative flux (c), sensible and latent heat flux (d) and (e), and the total net surface heat flux (f). Error bars are the mean standard errors of the computed seasonal cycle from a decade of KEO fluxes.
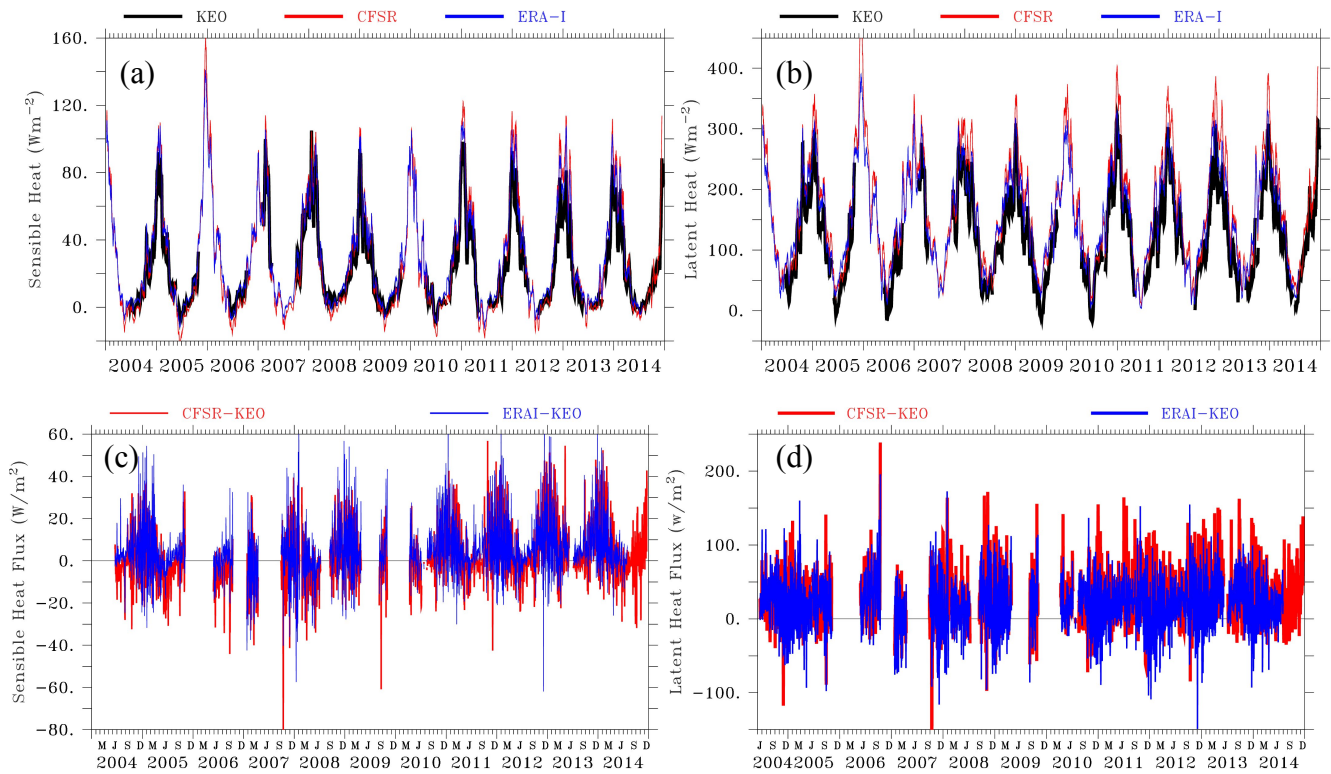
692

693 Figure 8: (a) and (b) Sensible and latent heat fluxes from KEO measurements, compared to the CFSR

694 and ERA-I reanalyses (15-day lowpass filtered to better show the timeseries); (c) and (d) Differences of

695 daily CFSR and ERA-I sensible and latent heat fluxes with KEO measurements.

696

697
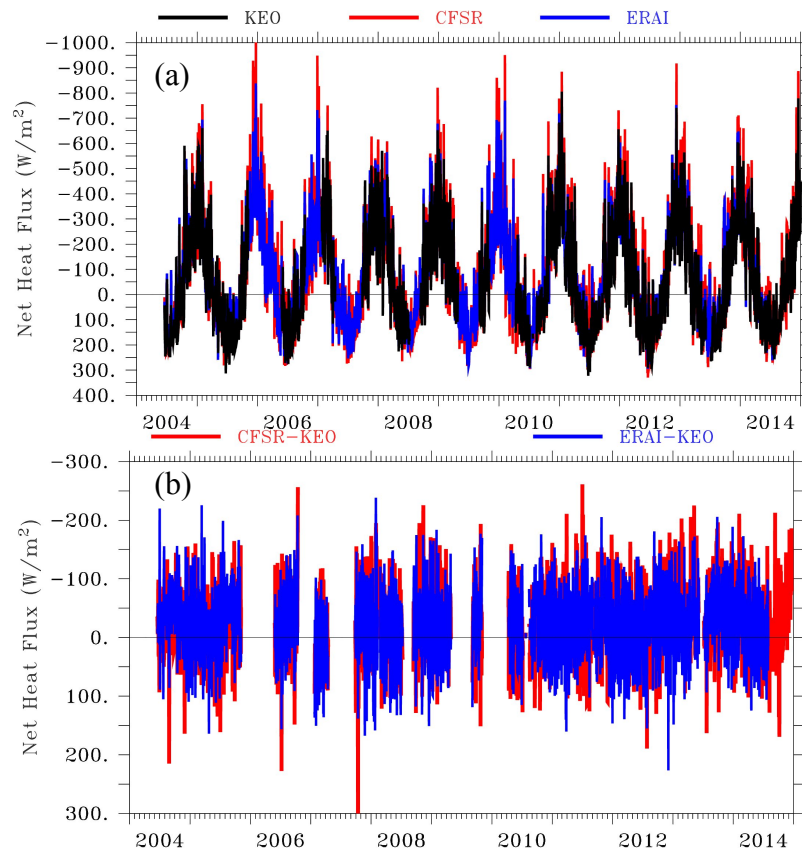
Figure 9 (a) Total daily net surface heat flux from KEO measurements, compared to the CFSR and ERA-I reanalyses; (b) Differences of daily CFSR and ERA-I net surface heat flux with KEO measurements.
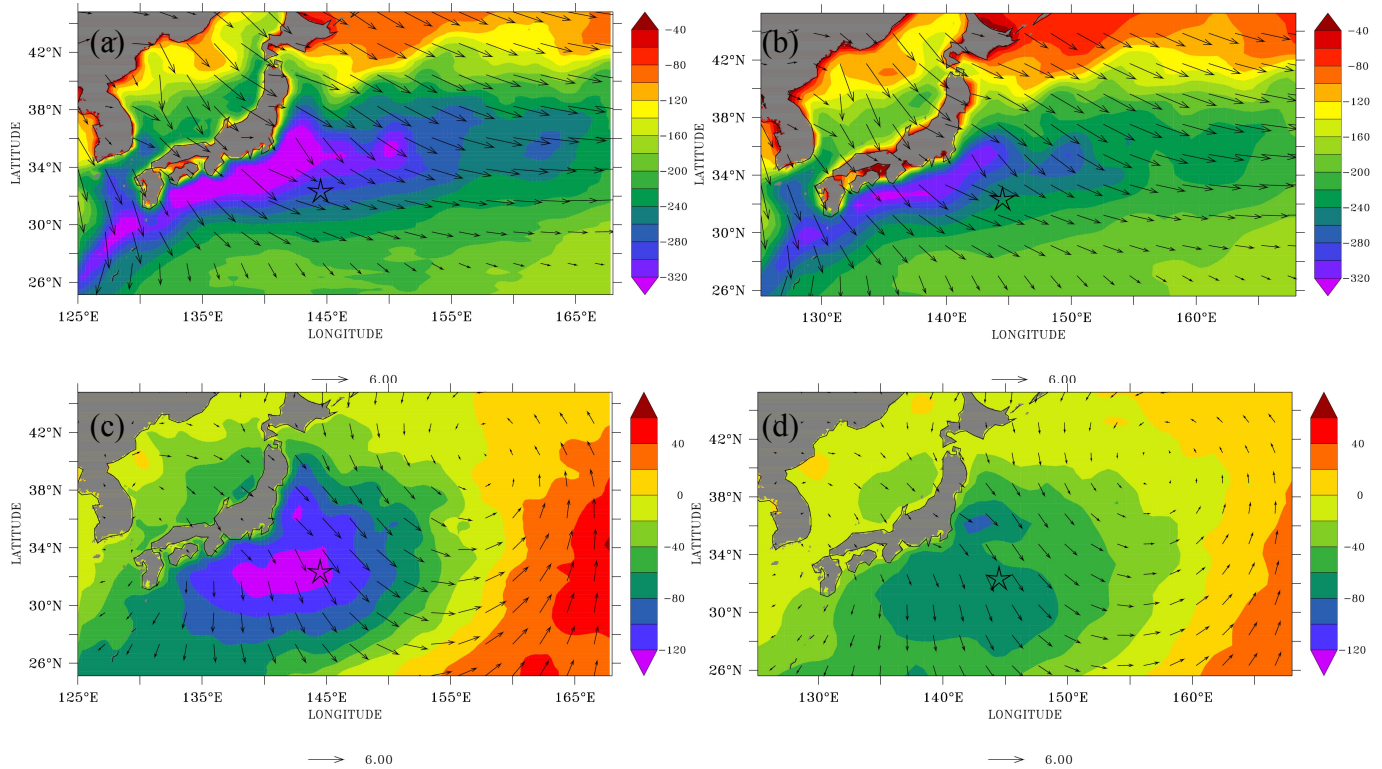
702 Figure 10: (a) and (b) Winter mean latent flux and wind vectors in CFSR and ERA-I during 2004-2014;

703 (c) and (d) Composites of cold anomalies due to synoptic weather events, showing patterns of winter

704 storms with low pressure center around 158°E, 40°N in the two reanalyses. The composites are

705 computed based on one standard deviation of the difference between daily and 21-day low-pass filtered

706 daily latent heat fluxes from KEO observation. The 21-day low-pass filter is used to filter out synoptic

707 weather events. Results are not sensitive to the length of filtering, tested between 15-day to 45-day.
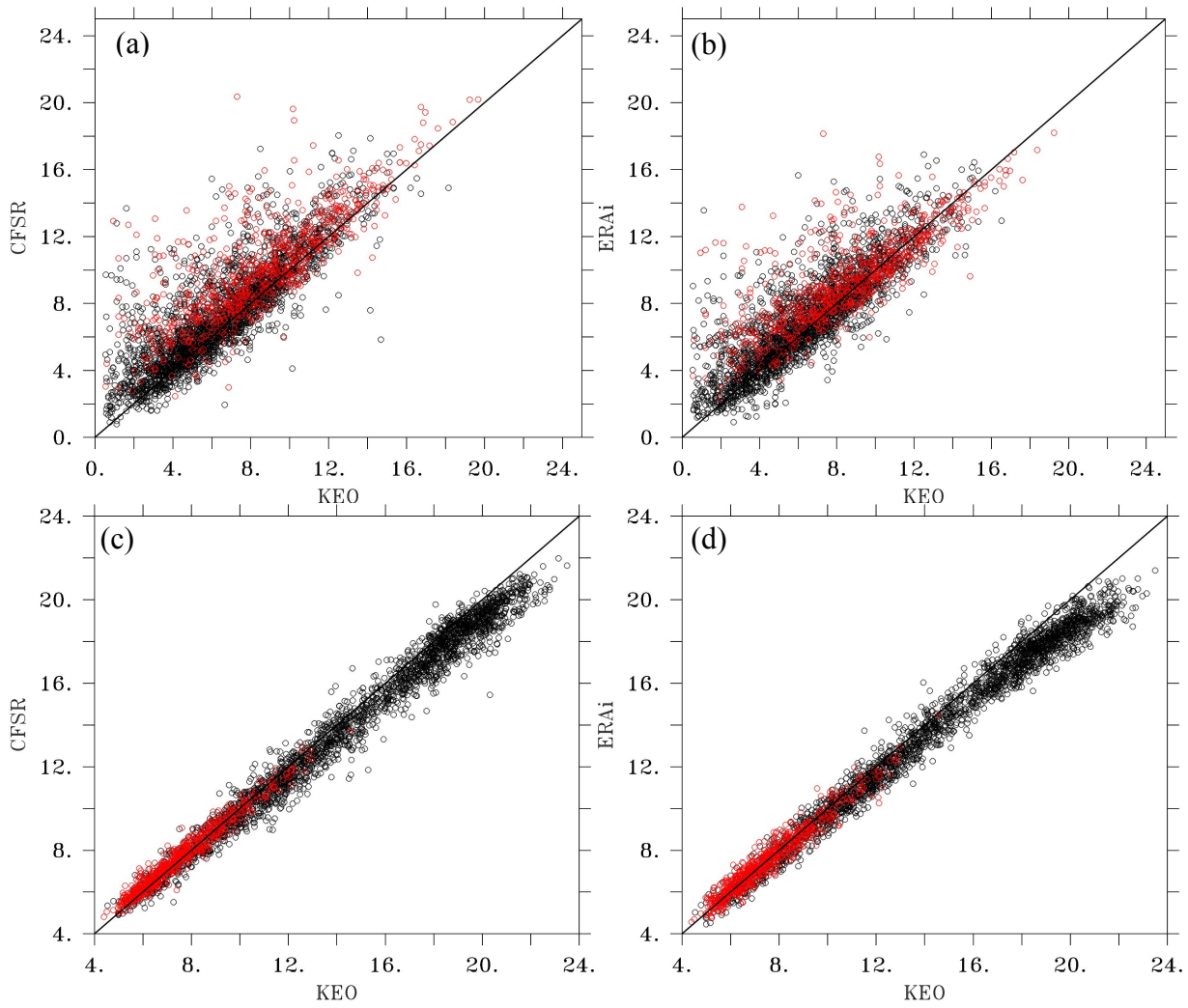
Figure 11: (a) and (b) Scatter plots of wind speed of KEO and reanalyses.; (c) and (d) Scatter plots of surface specific humidity q_a of KEO and reanalyses. Winter data are shown in red.
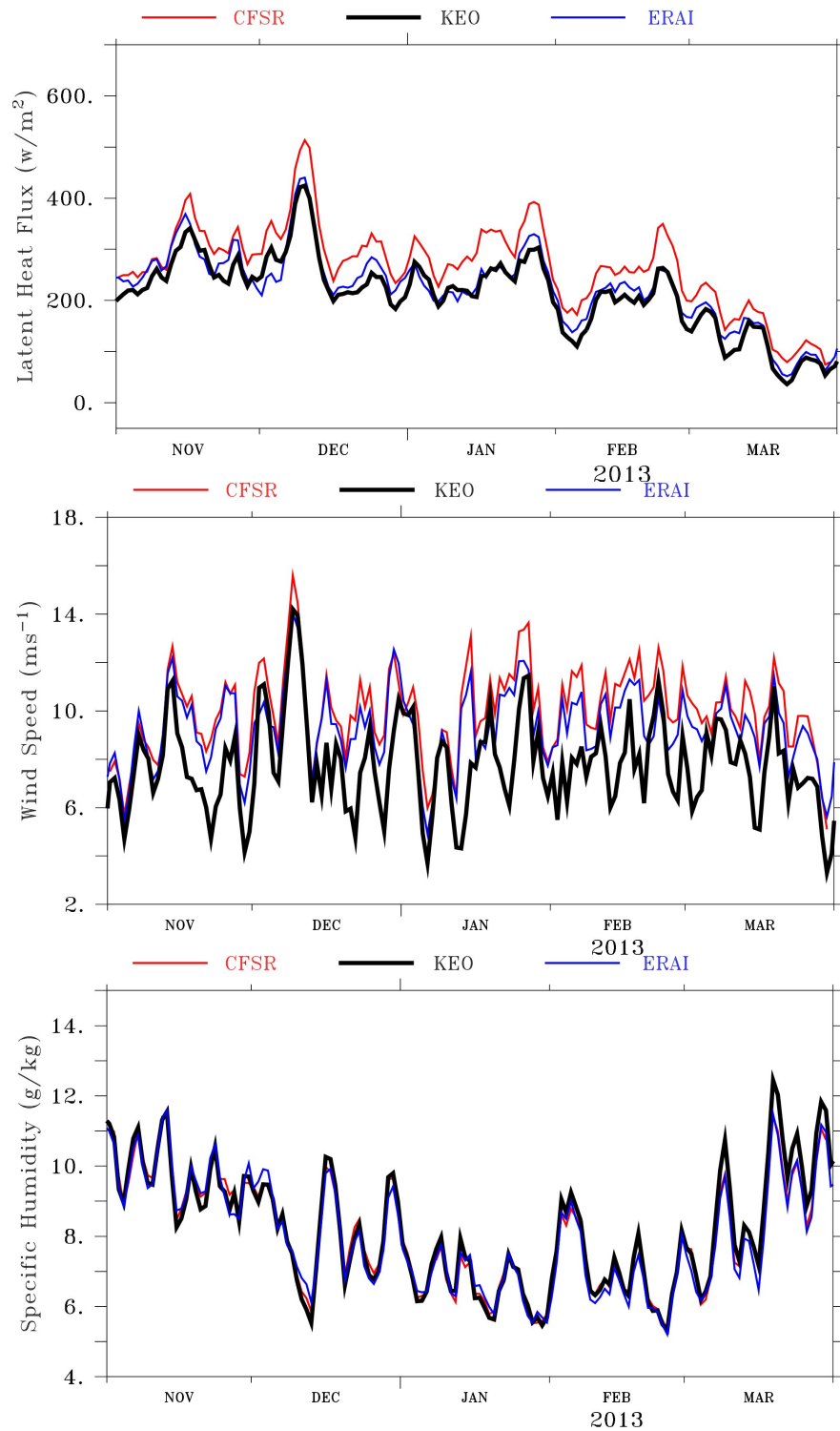
Figure 12: Latent heat flux, wind speed, and specific humidity during November 2012 to March 2013, 3-day lowpass filtered to better show the timeseries.
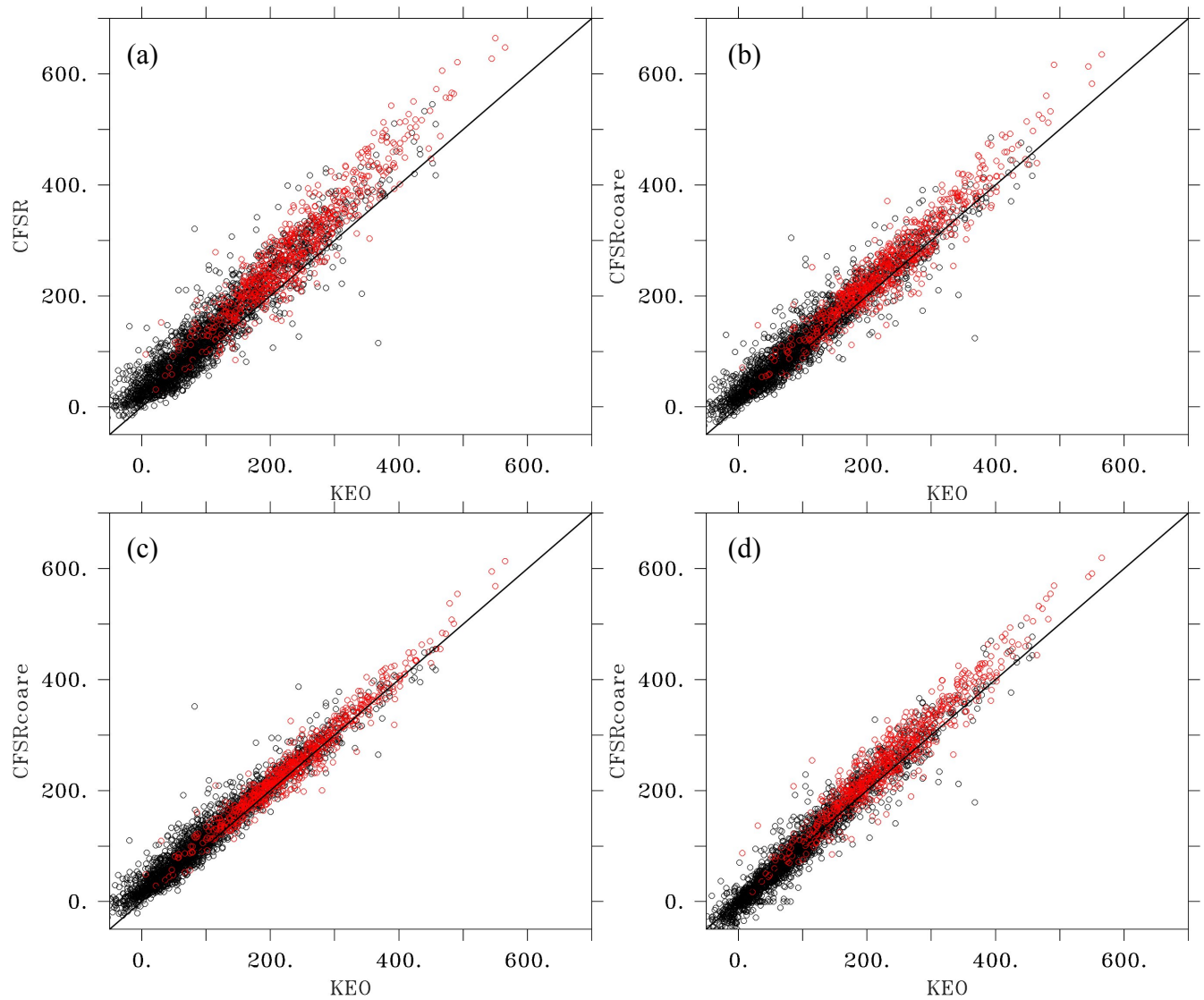
Figure 13: Scatter plots of latent fluxes of (a) KEO and CFSR; (b) KEO and CFSR using COARE 3.0b bulk algorithm; (c) KEO and CFSR using COARE 3.0b bulk algorithm and KEO wind speed; (d) KEO and CFSR using COARE 3.0b bulk algorithm and KEO specific humidity. Winter data points are shown in red.